

## Article

# Designing Highly Active S-g-C<sub>3</sub>N<sub>4</sub>/Te@NiS Ternary Nanocomposites for Antimicrobial Performance, Degradation of Organic Pollutants, and Their Kinetic Study

Maryam Ramzan<sup>1</sup>, Mohsin Javed<sup>1</sup> , Shahid Iqbal<sup>2,\*</sup> , Ahmad Alhujaily<sup>3</sup>, Qaiser Mahmood<sup>4</sup>, Komal Aroosh<sup>1</sup>, Ali Bahadur<sup>5,\*</sup> , Muhammad Abdul Qayyum<sup>6</sup> , Nasser S. Awwad<sup>7</sup> , Hala A. Ibrahim<sup>8</sup>, Murefah Mana Al-Anazy<sup>9</sup> and Eslam B. Elkaeed<sup>10</sup> 

- <sup>1</sup> Department of Chemistry, School of Science, University of Management and Technology, Lahore 54770, Pakistan
- <sup>2</sup> Department of Chemistry, School of Natural Sciences (SNS), National University of Science and Technology (NUST), H-12, Islamabad 46000, Pakistan
- <sup>3</sup> Biology Department, College of Science, Taibah University, P.O. Box 344, Al Madinah Al Munawarah 41477, Saudi Arabia
- <sup>4</sup> Chemistry and Chemical Engineering Guangdong Laboratory, Shantou 515031, China
- <sup>5</sup> Department of Chemistry, College of Science and Technology, Wenzhou-Kean University, Wenzhou 325060, China
- <sup>6</sup> Department of Chemistry, Division of Science & Technology, University of Education, Lahore 54770, Pakistan
- <sup>7</sup> Chemistry Department, Faculty of Science, King Khalid University, P.O. Box 9004, Abha 61413, Saudi Arabia
- <sup>8</sup> Biology Department, Faculty of Science, King Khalid University, P.O. Box 9004, Abha 61413, Saudi Arabia
- <sup>9</sup> Department of Chemistry, College of Science, Princess Nourah bint Abdulrahman University, P.O. Box 84428, Riyadh 11671, Saudi Arabia
- <sup>10</sup> Department of Pharmaceutical Sciences, College of Pharmacy, Almaarefa University, P.O. Box 71666, Riyadh 13713, Saudi Arabia
- \* Correspondence: shahidiqbal.chem@sns.nust.edu.pk (S.I.); abahadur@wku.edu.cn (A.B.)



**Citation:** Ramzan, M.; Javed, M.; Iqbal, S.; Alhujaily, A.; Mahmood, Q.; Aroosh, K.; Bahadur, A.; Qayyum, M.A.; Awwad, N.S.; Ibrahim, H.A.; et al. Designing Highly Active S-g-C<sub>3</sub>N<sub>4</sub>/Te@NiS Ternary Nanocomposites for Antimicrobial Performance, Degradation of Organic Pollutants, and Their Kinetic Study. *Inorganics* **2023**, *11*, 156. <https://doi.org/10.3390/inorganics11040156>

Academic Editors: Alejandro Pérez-Larios and Oomman K. Varghese

Received: 28 February 2023  
Revised: 25 March 2023  
Accepted: 31 March 2023  
Published: 3 April 2023



**Copyright:** © 2023 by the authors. Licensee MDPI, Basel, Switzerland. This article is an open access article distributed under the terms and conditions of the Creative Commons Attribution (CC BY) license (<https://creativecommons.org/licenses/by/4.0/>).

**Abstract:** The current research is about the synthesis of pure nickel sulfide, a series of Te (0, 0.5, 1, 1.5, 2, and 3 wt.%) -doped NiS (Te@NiS) nanoparticles (NPs), and a series of S-g-C<sub>3</sub>N<sub>4</sub> (10, 30, 50, 70, and 80 wt.%) /Te@NiS nanocomposites (NCs), fabricated through a hydrothermal route. XRD and FTIR spectroscopic techniques demonstrated the successful synthesis of NPs and NCs. SEM-EDX images confirmed the flakelike structure and elemental constituents of the fabricated materials. Tauc plots were drawn, to calculate the band gaps of the synthesized samples. Te doping resulted in a significant reduction in the band gap of the NiS NPs. The photocatalytic efficiency of the NPs and NCs was investigated against MB, under sunlight. The results obtained for the photocatalytic activity, showed that 1%Te@NiS nanoparticles have an excellent dye degradation capacity in sunlight. This was made even better by making a series of SGCN/1% Te@NiS nanocomposites with different amounts of S-g-C<sub>3</sub>N<sub>4</sub>. When compared to NiS, Te@NiS, SGCN, and 70%SGCN/1%Te@NiS, the 70%SGCN/1%Te@NiS NCs have excellent antifungal ability. The higher impact of SGCN/Te@NiS, may be due to its enhanced ability to disperse and interact with the membranes and intracellular proteins of fungi. The 70%SGCN/1%Te@NiS NCs showed excellent antibacterial and photocatalytic efficiency. Thus, the 70%SGCN/1%Te@NiS NCs might prove fruitful in antibacterial and photocatalytic applications.

**Keywords:** synthesis of NiS; synthesis of Te@NiS; synthesis of S-g-C<sub>3</sub>N<sub>4</sub>/Te@NiS nanocomposites; antibacterial study; photocatalytic activity

## 1. Introduction

The textile industry is an important contributor to the global economy. It accounts for a large part of global exports and creates many jobs. Still, it has also been regarded as a significant contributor to global pollution [1–4]. Most of the damage that the textile industry does to the environment, is caused by the discharge of untreated effluent into

waterways, which accounts for about 80% of all emissions from the industry [5–7]. The effluent discharged by the textile industry, is a combination of metals, dyes, and other pollutants [8]. Textile dyes are our biggest concern, because they are mutagenic, can cause cancer, and stay in the environment for a long time. They also affect whole food chains and bioaccumulate, which means that species higher up the food chain have higher levels of contamination than their prey [5,9–11]. In this regard, azo-type textile dyes deserve special attention, because during the dyeing process, approximately 15% to 50% of them are discharged into water that emerging countries regularly utilize for irrigation [12]. This water has negative impacts on the soil and living beings, and enters the food chain. Therefore, in order to preserve the sustainability of the ecosystem for future generations, remediation measures must be implemented [13–15].

Regarding solving problems that arise from textile effluent, semiconductor-based photocatalysts, such as metal oxides (e.g.,  $\text{TiO}_2$  [16,17],  $\text{ZnO}$  [18,19],  $\text{Bi}_2\text{WO}_6$  [20],  $\text{CuO}$  [21,22],  $\text{WO}_3$  [23], and  $\text{Fe}_2\text{O}_3$  [24]), metal sulfides (e.g.,  $\text{ZnS}$  [25,26],  $\text{CuS}$  [27,28],  $\text{CdS}$  [29,30],  $\text{Ag}_2\text{S}$  [31],  $\text{Bi}_2\text{S}_3$  [32], and  $\text{NiS}$  [33]), and chitosan coated zinc oxide (CS-ZnO) nanocomposites [34], have attracted wide attention because of their ability to degrade organic pollutants by utilizing solar energy [35–37], and for the production of hydrogen [38]. Among these photocatalysts, metal-sulfide-based semiconductors are the most well-known for degrading dyes with cost-effective, eco-friendly, and long-lasting treatment methods [39,40]. Among the metal sulfide photocatalysts,  $\text{NiS}$  plays an ideal role in the selection of p-type semiconductors, that match with the energy levels of  $\text{TiO}_2$  [41]. Furthermore, its binary Ni-S systems have more earth abundant resources, possessing multiple phases, such as  $\text{Ni}_3\text{S}_2$ ,  $\text{Ni}_9\text{S}_8$ ,  $\text{Ni}_7\text{S}_6$ ,  $\text{NiS}_2$ ,  $\text{Ni}_3\text{S}_4$ ,  $\text{NiS}$ , etc. [42].  $\text{NiS}_2$  nanostructures, including nanoparticles, hollow microspheres, nanowires, and nanosheets, have been hailed as potential semiconducting materials [43] for catalytic applications because of their stability, affordability, and nontoxic nature [42,44,45]. However, despite having optoelectronic properties [46], the efficiency of photodegradation remains low when using metal sulfides, due to the fast electron-hole recombination [47]. Similarly, photocorrosion and low quantum efficiency also affect metal sulfides. So, overcoming these issues before applying metal sulfides as photocatalysts, is necessary [48]. In this regard, enormous efforts have been undertaken, such as modifications to the structure of the nanoparticles, or doping.

Doping of high-surface-area particles or materials is required for increasing the photocatalytic performance and charge transfer characteristics of the catalyst [49]. Ceramic oxide nanodoping ( $\text{Al}_2\text{O}_3$ ,  $\text{TiO}_2$ ,  $\text{SiO}_2$ , etc.) can improve the dielectric characteristics of composites, while maintaining their high thermal durability [50]. Electrocatalytic  $\text{H}_2$  generation can be improved by doping with a non-noble metal catalyst. This helps to solve the issue of low efficiency related to the production of either metal electrocatalytic  $\text{H}_2$  or non-noble metal  $\text{H}_2$ . Previously, metal/nonmetal doping has been used to improve the morphology and characteristics of nanodoped  $\text{NiS}$ . Cobalt doping on nickel sulfide improves its efficiency to evolve electrocatalytic hydrogen [51].

Properly engineered heterojunctions/nanocomposites are the newest trend in nanostructured material development. They are characterized as a mixture of two or more phases with distinct structures and compositions, one of which is in the nanoscale regime [52].  $\text{NiS}$  is a p-type semiconductor, whereas  $\text{g-C}_3\text{N}_4$  is typically thought of as an n-type semiconductor. Both of these semiconductors' p-n heterostructures can aid in the promotion of charge transfer and separation [41,53]. The p-n heterostructures of both, can help to promote the charge transfer/separation [54,55]. Previous studies have also shown that the synergistic interactions between  $\text{g-C}_3\text{N}_4$  and the other parts of the heterostructures, inhibit the recombination of photogenerated charge carriers and give the photocatalysts some unique properties [56]. A photocatalyst consisting of  $\text{NiS/g-C}_3\text{N}_4/\text{SrTiO}_3$  (NS/CN/STO) was prepared using a hydrothermal method. The combination of the CN/STO heterojunction and  $\text{NiS}$  cocatalyst, resulted in enhanced photocatalytic hydrogen evolution activity in the NS/CN/STO system [57]. A p-n heterostructured  $\text{NiS/BiVO}_4$  ( $\text{NiS/BVO}$ ) photocatalyst was designed, by pairing  $\text{NiS}$  (p-type) nanoparticles with nanostructured BVO (n-type),

and used to photodegrade an organic anion dye, in Li et al. The light harvesting and the separation and transfer of electrons were improved. A molar ratio of 0.7 for NiS/BVO, gave the highest photocatalytic capability, of 95.6%, within 90 min of irradiation, and a degradation rate of  $1.7970 \text{ h}^{-1}$  was achieved, which was almost 16 and 33 times greater than pure BVO and NiS, respectively [58]. Vignesh et al. developed the magnetically separable  $\text{g-C}_3\text{N}_4/\alpha\text{-Fe}_2\text{O}_3$  nanocomposite, for the photocatalytic degradation of mixed RhB and MB pollutants. They observed that the NC exhibited better photocatalytic efficiency than  $\text{g-C}_3\text{N}_4$  and  $\alpha\text{-Fe}_2\text{O}_3$  [59].

We first describe the hydrothermal synthesis process of sulfur-doped graphitic carbon nitride composites with Te@NiS nanoparticles (SGCN/Te@NiS), and then study their photocatalytic and antibacterial activity. In the current work, initially, NiS NPs were doped with a series of weight percentages of Te (0.5, 1, 1.5, and 3%) to improve their photocatalytic efficiency. In the photocatalytic MB degradation experiment, 1%Te@NiS NPs exhibited the best catalytic activity. Next, 1%Te@NiS NPs were homogenized with S-g-C<sub>3</sub>N<sub>4</sub>. The weight percentages of S-g-C<sub>3</sub>N<sub>4</sub>, in a series of S-g-C<sub>3</sub>N<sub>4</sub>/Te@NiS nanocomposites, were 10, 30, 50, 70, and 80 wt.%. The photocatalytic and antibacterial activity of the S-g-C<sub>3</sub>N<sub>4</sub>/Te@NiS composite was found to be better than that of Te@NiS and S-g-C<sub>3</sub>N<sub>4</sub>. Te doping in the NiS matrix and simultaneous coupling with S-g-C<sub>3</sub>N<sub>4</sub>, were primarily responsible for this improvement. A logical photocatalytic mechanism has also been postulated for the synthesized composite's enhanced photocatalytic and antibacterial activities under sunlight irradiation.

## 2. Experimental

### 2.1. Chemicals

The chemical reagents required for the synthesis of NiS, SGCN, Te@NiS nanoparticles, and the SGCN/Te@NiS nanocomposite, and for photocatalytic activity, were thiourea ( $\text{CH}_4\text{N}_2\text{S}$ ), nickel nitrate hexahydrate ( $\text{Ni}(\text{NO}_3)_2 \cdot 6\text{H}_2\text{O}$ ), sodium dodecyl sulfate (SDS) ( $\text{C}_{12}\text{H}_{25}\text{O}_4\text{S} \cdot \text{Na}$ ), methylene blue (MB) ( $\text{C}_{16}\text{H}_{18}\text{C}_1\text{N}_3\text{S}$ ), ethanol (for washing only) ( $\text{C}_2\text{H}_5\text{OH}$ ), and tellurium (Te). Nutrient broth and nutrient agar were used in the antibacterial study. All chemicals/reagents were used as purchased.

### 2.2. Synthesis of NiS and Te@NiS Nanoparticles

The NiS nanoparticles were assembled using a modified version of a previously reported hydrothermal technique. The typical synthesis experiment involved preparing two solutions: solution "A" was prepared by dissolving 0.75 g of thiourea into 10 mL of distilled water, under magnetic stirring. Nickel nitrate hexahydrate (1.63 g) and 1 g of sodium dodecyl sulfide, were added to 15 mL of distilled water, under constant stirring. This solution was marked as solution "B." Then, solutions A and B were mixed in one beaker, and constantly stirred for about 20 min. Next, this solution was transferred into a 25 mL Teflon-lined, sealed stainless autoclave. The autoclave was kept in an oven at  $80 \text{ }^\circ\text{C}$  for about 8 h. Greyish-black precipitates were obtained and ground into powder. Following filtering and rinsing with water/ethanol, the residues were dried in an oven at  $70 \text{ }^\circ\text{C}$ , for two hours. A series of weight percentages of Te (0.5, 1, 1.5, and 3%) was doped into NiS nanoparticles, employing the same process, except for varying the tellurium concentration.

### 2.3. Synthesis of SGCN

To fabricate SGCN nanosheets by simple means of calcination, 10 g of thiourea was placed in a covered alumina crucible and calcined in a muffle furnace. The temperature was raised progressively until it reached  $550 \text{ }^\circ\text{C}$ , and then that temperature was maintained for about 4 h. The resulting yellowish product was cooled and then ground into a fine powder [60].

#### 2.4. Synthesis of SGCN/Te@NiS Nanocomposites

The Te@NiS NPs were modified by integrating 0.11, 0.34, 0.63, 0.84, and 0.93 g of SGCN, to prepare 10, 30, 50, 70, and 80 wt.% nanocomposites. To synthesize 70 wt.% SGCN/Te@NiS composites, 1.22 g of nickel nitrate hexahydrate and 1 g of sodium dodecyl sulfide were dissolved in 15 mL of distilled water, with constant stirring at room temperature (solution A). Solution “B” was prepared by dissolving 0.75 g of thiourea, 0.014 g of tellurium powder, and 0.84 g of SGCN. After that, the two solutions were put into one beaker and constantly stirred for about 20 min. Then, that solution was poured into a 25 mL Teflon-lined autoclave and placed in an oven at 200 °C, for about 8 h. The greyish-black residue obtained, was dried at 80 °C for 2 h. Later on, the composite was collected and stored for characterization. Other nanocomposites were prepared in a similar fashion. Figure 1 depicts a schematic diagram for the fabrication of the nanocomposites.

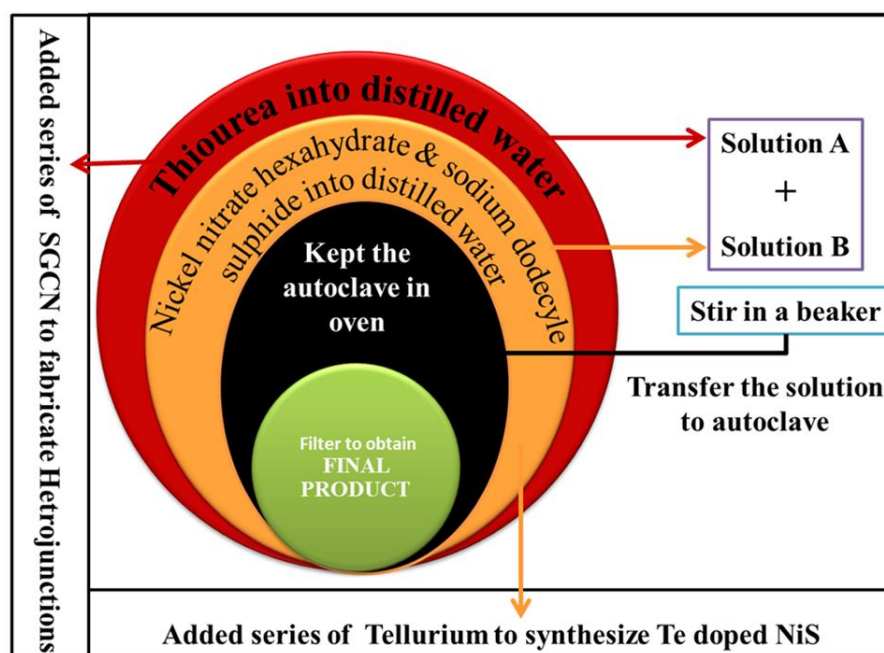


Figure 1. Schematic diagram for the synthesis of nanoparticles.

#### 2.5. Photocatalytic Study

A volume of 100 mL of MB aqueous solution was mixed with 0.2 g of each material. in a typical photocatalytic experiment. The mixture was left to stir in the dark for around 30 min, to reach the adsorption–desorption equilibrium. After that, the suspension was placed in an open environment, with sunlight, and the degradation of the MB dye was checked by taking 5 mL aliquots at regular intervals (30 min). After centrifuging these aliquots, a UV-visible spectrophotometer was used to record the samples’ absorption spectra. In order to determine the rate constant for degradation,  $k$ , from the first-order plot, it was hypothesized that the rate of degradation would follow pseudo-first-order kinetics (Equation (1)).

$$\ln\left(\frac{A_0}{A}\right) = kt \quad (1)$$

where  $A_0$  is the initial absorbance,  $A$  is the absorbance after a time ( $t$ ), and  $k$  is the pseudo-first-order rate constant.

The percentage degradation efficiency of the polluted dyes was studied using Equation (2):

$$\text{Degradation \% age efficiency} = \frac{A_0 - A_e}{A_0} \times 100 \quad (2)$$

### 2.6. Band Gap Calculations for Photocatalysts

The band gap was calculated by using UV-visible spectroscopy, to measure the absorbance of samples, and then converting the absorbance data into a Tauc plot. The Tauc plot was drawn with energy on the x-axis and  $(\alpha h\nu)^2$  on the y-axis. The calculation involves the following equation:

$$(\alpha h\nu)^\gamma = A(h\nu - E_g) \quad (3)$$

where,  $h\nu$  is easily calculated by

$$h\nu = \frac{1240}{\lambda(\text{nm})} \quad (4)$$

and  $\alpha$  is calculated by the Beer-Lambert equation

$$\alpha = \frac{4\pi A}{\lambda(\text{nm})} \quad (5)$$

### 2.7. Antimicrobial Study

Antimicrobial activities were carried out with the best photocatalytic activity NPs and NCs. The Antimicrobial activity determination was carried out using the agar-well diffusion method. The process that was followed is described below:

1. The cultured bacteria and fungi were used to prepare inoculum. Two flasks were taken, having 25 mL water each with 0.32 g of nutrient broth. The flasks were autoclaved for about 15 min and labeled with the name of bacterial strains, i.e., *Bacillus subtilis* (*B. subtilis*) and *Escherichia coli* (*E. coli*) and fungi strains i.e. *Monilinia laxa* (*M. laxa*) and *Fusarium oxysporum* (*F. oxysporum*). Two drops of bacterial strain were added into the respective flasks and placed in a shaker for 24 h. The fungal strains were incubated for 48 h.
2. Then, the photocatalyst solutions (mg/L) were prepared, by using the relation:  $M_1V_1 = M_2V_2$
3. The medium was prepared by adding 1 g agar and 2 g broth to 100 mL water, in a flask. The solution was heated until it boiled. The sample was poured into Petri dishes and was allowed to cool down and solidify.
4. After cooling, holes were punched in the gel by hole puncture, according to the number of mg/L solutions prepared (blank, 100 ppm, 200 ppm, 300 ppm, 400 ppm, 500 ppm). The prepared mg/L solutions were added into the respective holes. The Petri dishes were covered and incubated for about 24 h at 37 °C and at 28 °C for 48 h for fungal strains.

## 3. Results and Discussion

### 3.1. Fourier-Transform Infrared Spectroscopy (FTIR)

FTIR spectroscopy was employed to analyze the functional groups present in the samples. The FTIR spectrum of NiS (Figure 2a), revealed a stretching vibration of –OH at approximately 3261.7  $\text{cm}^{-1}$  and at around 3116.9  $\text{cm}^{-1}$  for 1%Te@NiS, showing the presence of water. The occurrence of strong adsorption peaks for Te@NiS in a lower frequency range, at 973 and 609  $\text{cm}^{-1}$ , is an indication of the successful incorporation of tellurium into the NiS NPs (Figure 2b). The stretching modes of the C–H group have been attributed to the bands appearing at approximately 2949.6 and 2919.02  $\text{cm}^{-1}$ . A distinct absorption band at 973  $\text{cm}^{-1}$  was identified as a specific peak for the Ni–S bond. The development of a metal–sulfur coordination bond was confirmed by the lower C=S shift stretching frequency at 609.9  $\text{cm}^{-1}$ . These peaks showed a slightly greater sharpness, and wavenumbers that are almost identical to the absorption bands of NiS. The FTIR spectrum of SGCN (Figure 2c), showed a sharp and prominent absorption band at 808  $\text{cm}^{-1}$ , that is assigned to the stretching mode of the triazine group. The presence of C–N heterocycles and their vibrational stretching, is indicated by the absorption bands detected in the range of 1228–1616  $\text{cm}^{-1}$ . A broad band at 3111  $\text{cm}^{-1}$ , is probably attributable to O–H bond

stretching and uncondensed amine groups. These observed peaks agree with earlier reported research [61]. Specific peaks at 2923.2, 1631.2, and 1315.7  $\text{cm}^{-1}$  in the composite spectrum, correspond to Te@NiS peaks, while peaks at 1242.3, 1452.2, and 1542.2  $\text{cm}^{-1}$ , correspond to SGCN's absorption bands. This demonstrates that the SGCN/Te@NiS nanocomposite was successfully synthesized (Figure 2d).

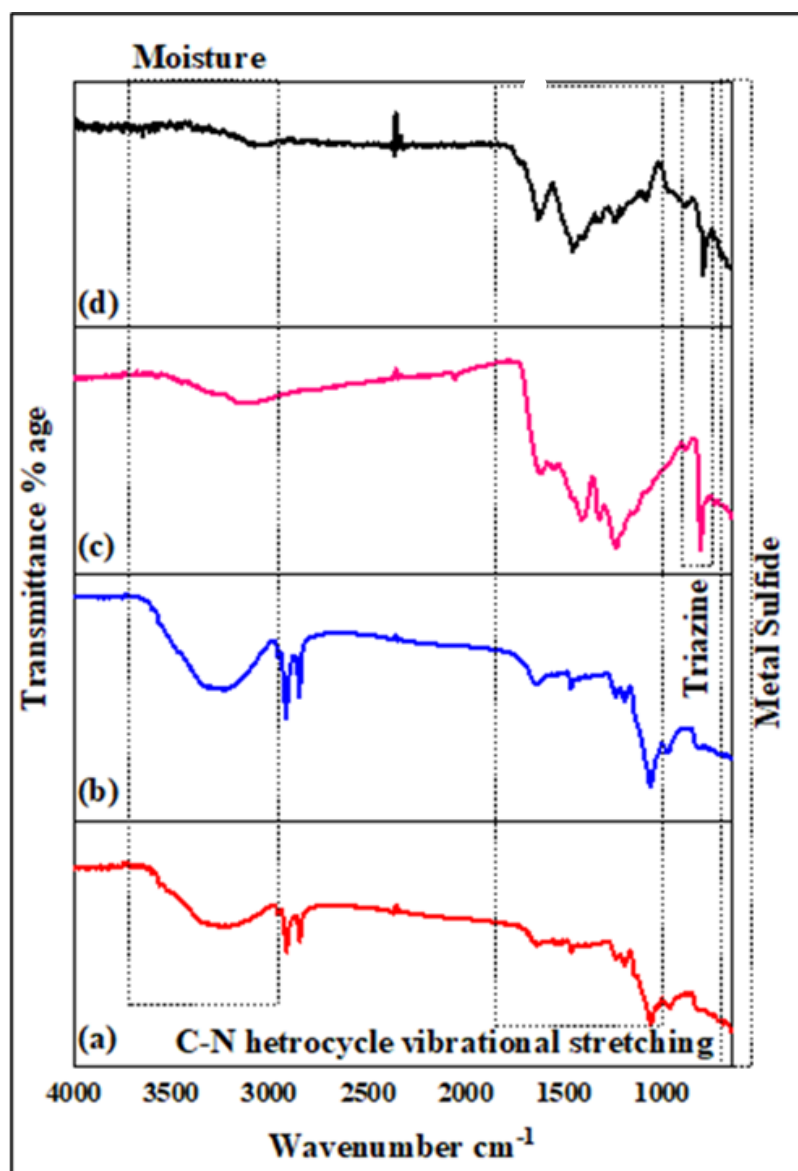


**Figure 2.** FTIR spectra of synthesized samples (a) NiS, (b) Te@NiS, (c) SGCN, and (d) SGCN/Te@NiS.

### 3.2. X-ray Diffraction Pattern

X-ray diffractograms were used to distinguish the phase, and lattice parameters of the synthesized photocatalysts (NiS, Te@NiS, SGCN, and SGCN/Te@NiS). The XRD pattern of nickel sulfide showed peaks at  $2\theta = 30.70^\circ, 32.62^\circ, 36.07^\circ, 38.36^\circ, 40.94^\circ, 49.38^\circ, 50.21^\circ, 52.73^\circ, 56.67^\circ, 57.89^\circ, 60.08^\circ, 71.09^\circ,$  and  $73.08^\circ$ , which correspond to the 101, 300, 021, 220, 211, 131, 410, 401, 321, 330, 312, and 431 crystalline planes of NiS (Figure 3a). The most intense peak was found at angle  $2\theta = 46.22^\circ$ . These outcomes were consistent with earlier work [62]. The XRD patterns of Te@NiS and SGCN/Te@NiS, show a minor shift towards the lower angles, demonstrating the effective doping of Te into NiS and the coupling of SGCN with Te@NiS photocatalysts, respectively (Figure 3b). These findings show that nickel has been adequately replaced by tellurium in the NiS lattice. Figure 3c shows the XRD pattern

for SGCN has two distinct peaks, at  $13.52^\circ$  and  $27.2^\circ$ , having facets of crystals (100) and (002), respectively. Figure 3c shows the XRD pattern for SGCN, with a distinct peak at  $13.52^\circ$ , having the facet of crystal (100). In the X-ray diffractogram of SGCN@Te/NiS, the distinct peaks obtained at  $2\theta = 11.42^\circ$ ,  $28.28^\circ$  are due to SGCN, while other peaks observed ( $31.73^\circ$ ,  $34.22^\circ$ ,  $37.83^\circ$ ,  $38.59^\circ$ ,  $40.93^\circ$ ,  $50.33^\circ$ ,  $51.75^\circ$ ,  $53.98^\circ$ ,  $56.47^\circ$ ,  $57.49^\circ$ ,  $60.13^\circ$ ,  $70.79^\circ$ , and  $72.77^\circ$ ), correspond to the crystalline planes of Te@NiS.

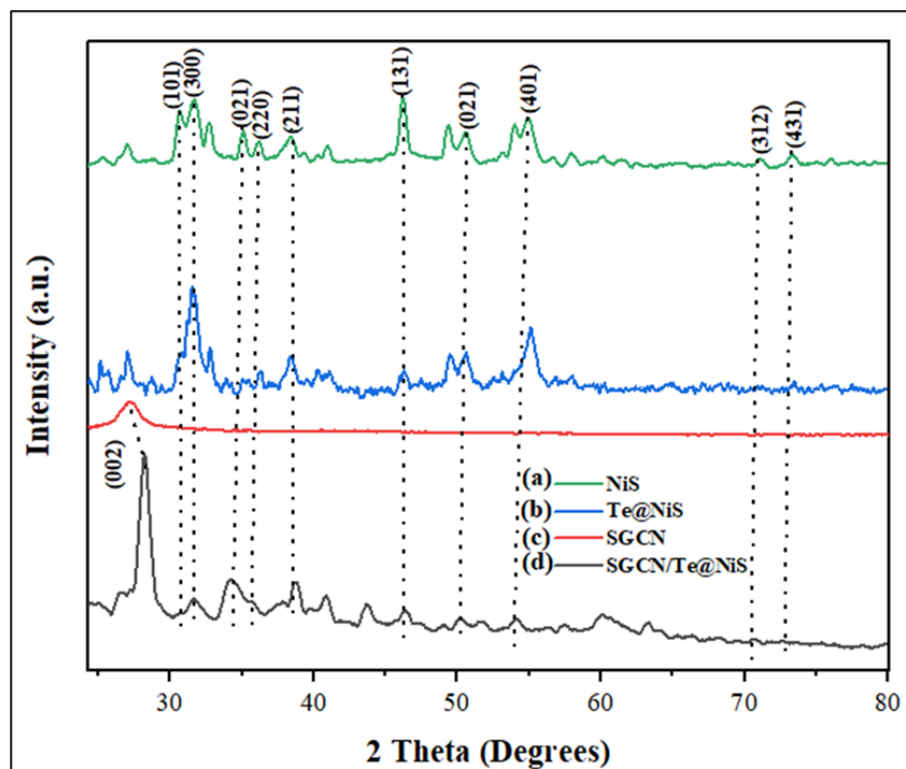


**Figure 3.** XRD pattern of (a) NiS, (b) Te@NiS, (c) SGCN, and (d) SGCN/Te@NiS.

### 3.3. SEM

Figure 4 displays SEM images showing the morphological structure of NiS, Te@NiS NPs, and SGCN/Te@NiS NCs. Figure 4a,b show SEM images of NiS at two different magnifications. In these images, NiS showed a two dimensional flakelike structure. In Figure 4c,d, the agglomerated Te@NiS nanoparticles can be seen in various sizes. Two distinct magnifications of SGCN/Te@SGCN are shown in Figure 4e,f. The images reveal that the agglomerated flakes found in the Te@NiS NPs, are aligned on the surface of the SGCN sheets. The EDX spectrum of SGCN/Te@NiS (Figure 4g), revealed the existence of carbon (C), nitrogen (N), nickel (Ni), oxygen (O), tellurium (Te), and sulfur (S). The percentage composition of the components found in the SGCN/Te@NiS composite was in the order  $\text{Ni} > \text{C} > \text{O} > \text{S} > \text{Te}$ . This demonstrates that C and O have greater content ratios, whereas Te has the lowest concentration. The detected elements in the EDX spectrum, confirm the successful synthesis of SGCN/Te@NiS.

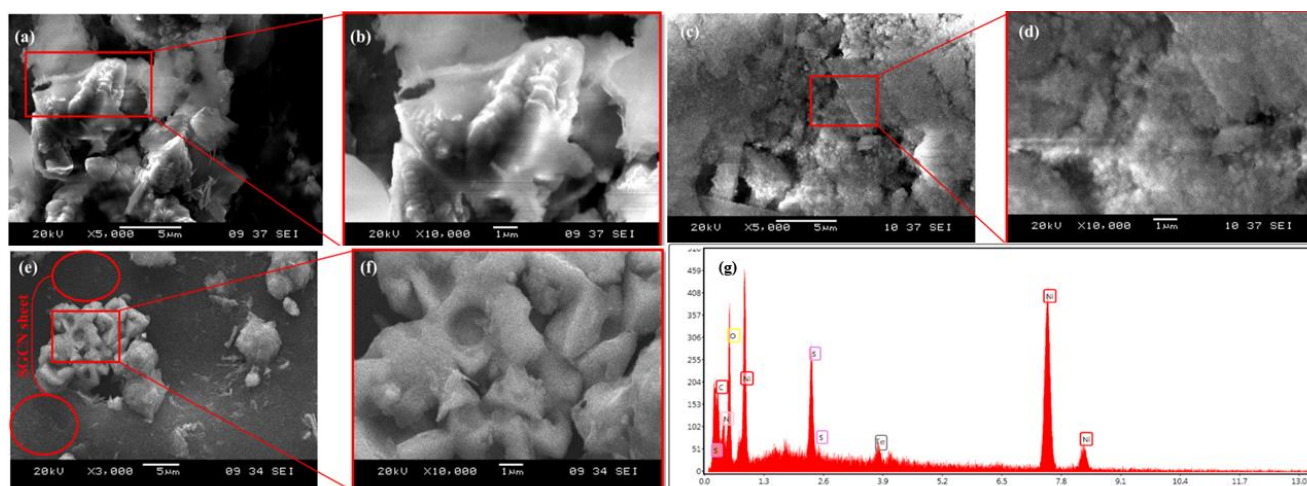


**Figure 4.** SEM images of (a,b) NiS, (c,d) Te@NiS, and (e,f) SGCN/Te@NiS. (g) EDX spectrum of SGCN/Te@NiS composite.

### 3.4. Band Gap

The band gap is the key property for determining the photocatalytic performance of the synthesized samples. The calculated band gap for NiS is about 3.70 eV [63] (Figure 5a), which decreases to 3.23 eV on doping with Te (Figure 5b), confirming the massive reduction in  $e^-/h^+$  pair recombination rate, resulting in an increase in the photodegradation efficiency of MB. The calculated band gap for SGCN is 2.67 eV (Figure 5c). This energy bandgap of SGCN is similar to that previously reported [64]. A further decrease in the band gap (to 2.60 eV) was observed, by the hybridization of SGCN with Te@NiS (Figure 5d). It was deduced from the results, that the photogenerated  $e^-$  can easily jump from the impure state to the conduction band, or from the valence band to the impure state. In other words, the photodegradation efficiency of NiS NPs is enhanced by the formation of composites.

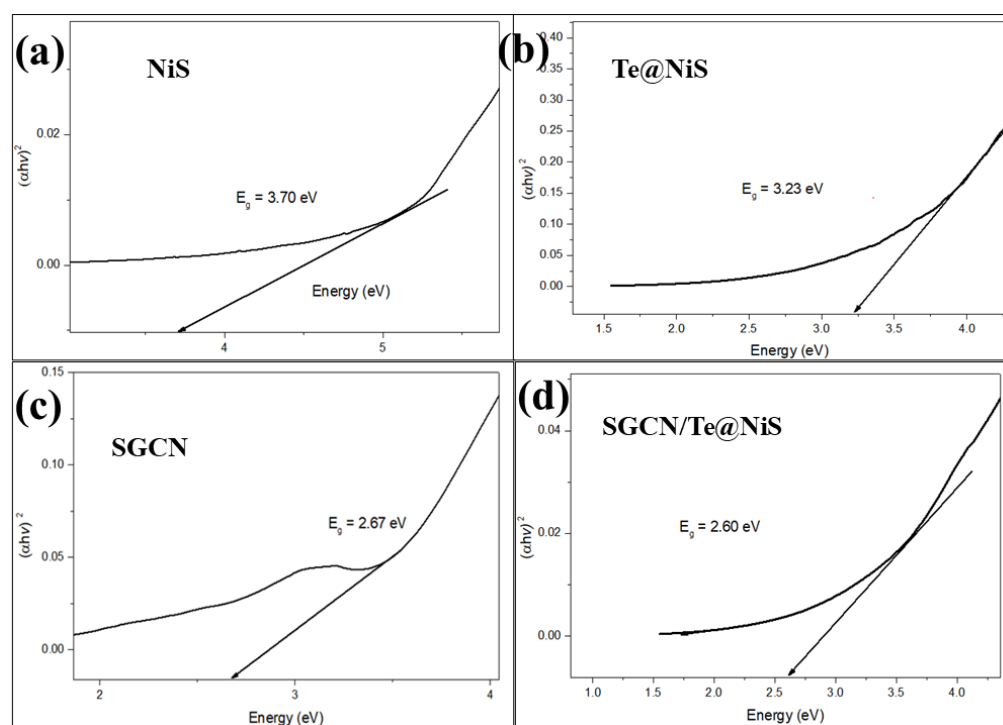


**Figure 5.** Tauc plots for band gap calculations (a) NiS, (b) Te@NiS, (c) SGCN, and (d) SGCN/Te@NiS.

### 3.5. XPS

XPS was used to analyze the surface chemistry of SGCN/Te@NiS, as well as the interaction between SGCN and Te@NiS. The binding energy at 283.3 eV might be attributed to the C–C coordination of the surface adventitious carbon, while that at 284.8 eV corresponds to sp<sup>2</sup>-bonded carbon, according to the high-resolution spectrum of C 1s (Figure 6a) (C–NH<sub>2</sub>). This shift was attributed to the interactions between SGCN and Te@NiS, since the binding energies of C 1s for SGCN/Te@NiS NCs, were somewhat lower than the published values for SGCN [65,66]. The graphitic N, pyrrolic N, and pyridine N could each be identified by one of three different peaks, at 402.5, 399.1, and 397.6 eV, in the SGCN N 1s peak. When compared to the previously published value for SGCN (398.5 eV), the binding energy of pyridine N in the SGCN/Te@NiS sample was reduced by 0.18 eV, thus demonstrating the interfacial contact between SGCN and Te@NiS (Figure 6b) [67,68]. Four characteristic peaks, of Te 3d<sub>5/2</sub> (573.21 eV), Te 3d<sub>3/2</sub> (583.21 eV), and TiO<sub>x</sub> (576.71 and 587.04 eV), were assigned to the metallic Te and tellurium ions, Te<sup>4+</sup>, in the Te 3d XPS spectrum (Figure 6c), which fully corresponds with the literature. The Ni 2p<sub>3/2</sub> and Ni 2p<sub>1/2</sub> can be ascribed to the peaks that occurred at 853.34 eV and 870.74 eV, respectively, in the Ni 2p spectrum of SGCN/Te@NiS (Figure 6d). Furthermore, the signal's satellite peaks, occurring at 862.41 and 880.24 eV, are similar to those noted elsewhere in the literature. Additionally, as shown in Figure S1, the deconvoluted XPS spectrum of the S 2p was performed for SGCN/Te@NiS, to analyze the valence state of the S. In SGCN/Te@NiS NCs, sulfur is generally associated with two distinct peaks, at 159.93 and 160.13 eV.

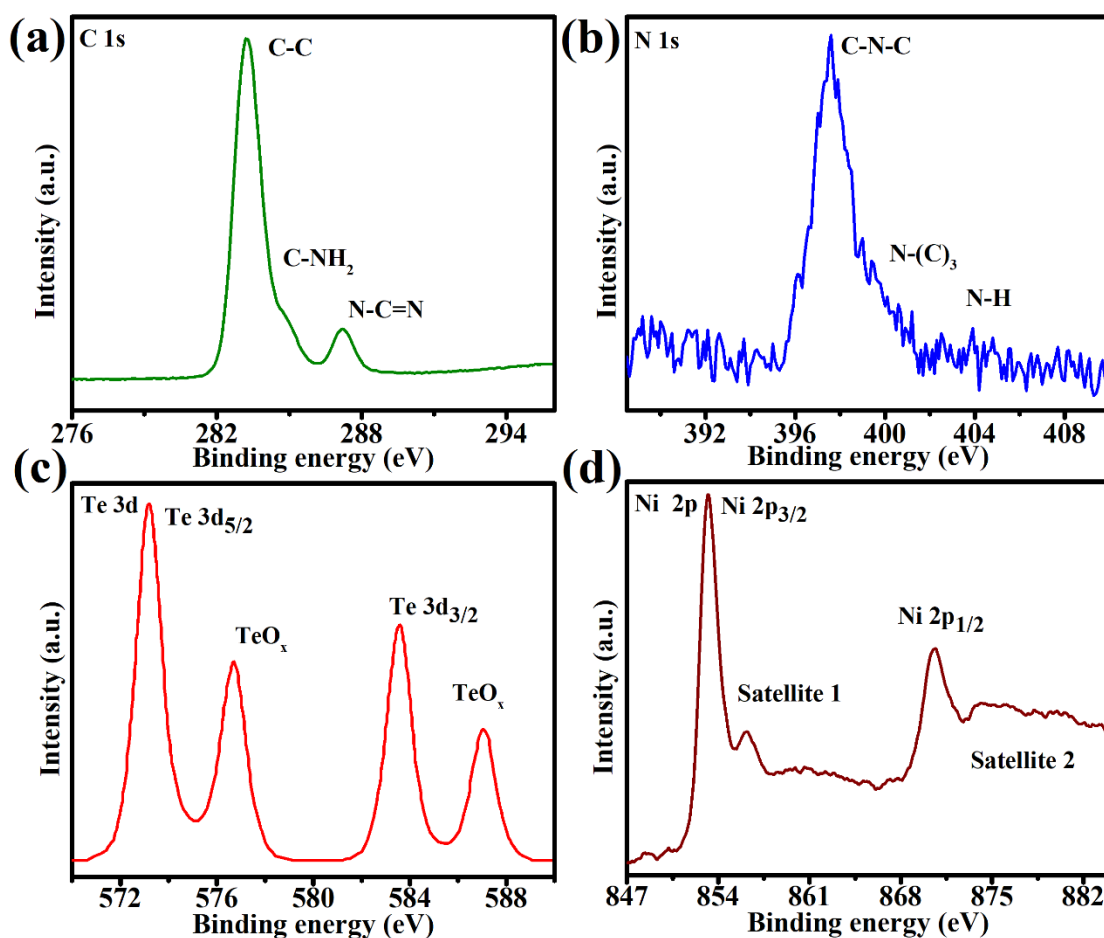


Figure 6. High-resolution XPS spectra of 70%SGCN/1%Te@NiS NCs: (a) C 1s, (b) N 1s, (c) Te 3d, and (d) Ni 2p.

### 3.6. Photocatalytic Activity Measurements

Using a UV-visible spectrophotometer, the photodegradation of methylene blue by pure NiS, Te@NiS nanoparticles, and SGCN/Te@NiS nanocomposites was observed under sunlight. The organic dye, methylene blue, was degraded by the synthesized nanocatalysts, resulting in the formation of the inorganic species H<sub>2</sub>O and CO<sub>2</sub>. UV-visible spectrophotometer results are shown in Figure 7a,b. The rate of degradation of methylene blue was found to be wavelength dependent. A high rate of degradation was observed in the visible region, at ~664 nm, and a low rate was found in the UV region, at ~292 nm (Figure 7c). The absorption strength reduced over time, which aided in increasing the photodegradation of methylene blue (Figure 7c). In the series of doped photocatalysts, the 1%Te@NiS nanoparticles were found to show excellent degradation of MB dye, as compared to other Te@NiS nanoparticles (Figure 7a,b), due to the synergistic photocatalytic effect of both Te metal and NiS. The decrease in the bandgap due to Te doping, helps to increase the charge separation and degradation rate of the MB dye. Thus, the degradation rate of MB increased for Te@NiS NPs, as compared to NiS NPs, and 1%Te@NiS exhibited the best photocatalytic activity. Next, 1%Te@NiS nanoparticles were integrated with SGCN (10, 30, 50, 70, and 80 wt.%), to develop more effective nanocomposites, and their photocatalytic activity against MB was examined.

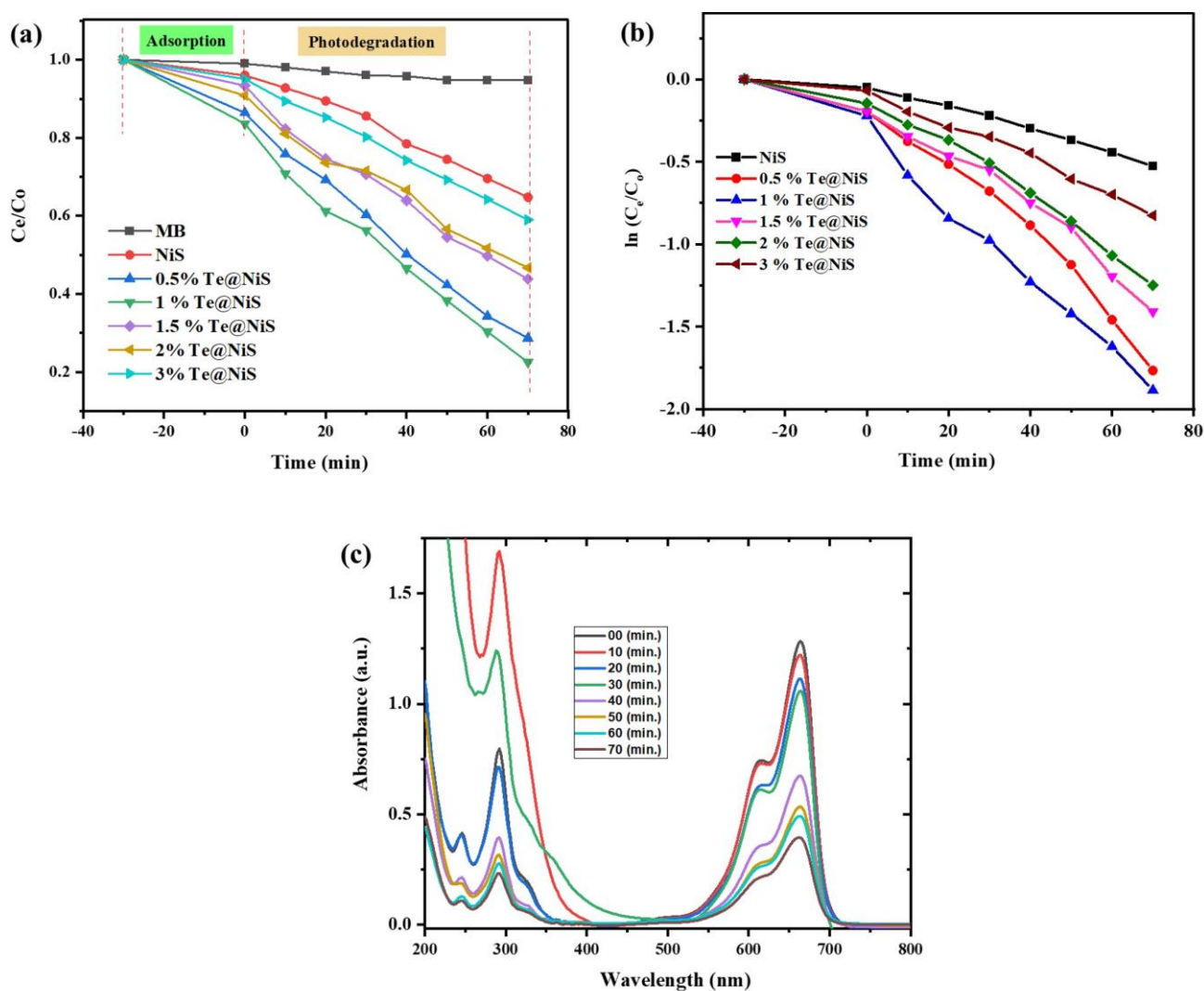
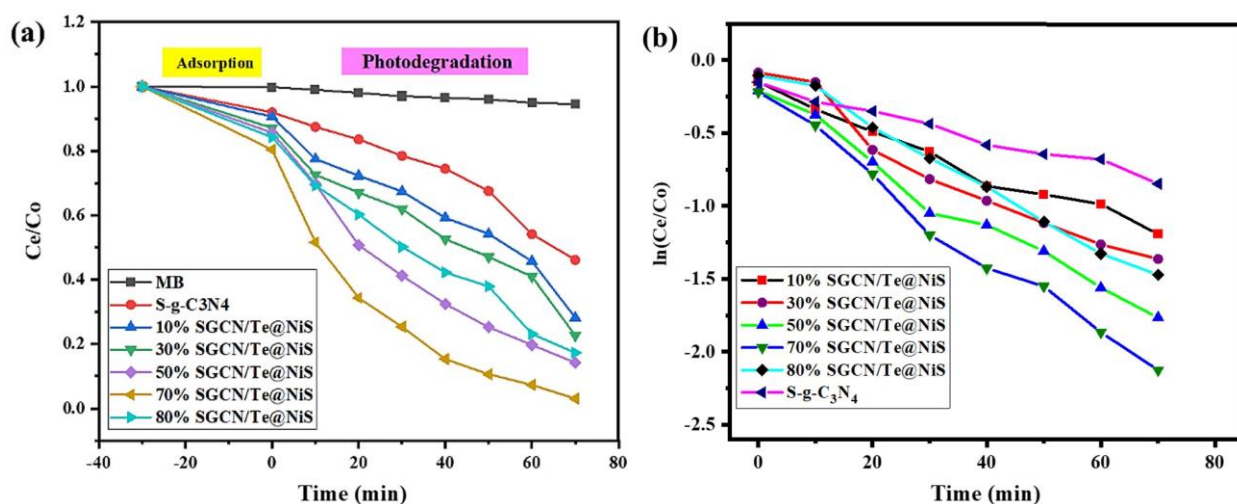


Figure 7. Degradation efficiency (a). Kinetic study (b). Effect of time on degradation of MB by Te@NiS NPs (c).

From the photocatalytic activity of the prepared series of nanocomposites, it was observed that, as the proportion of SGCN increased, so did the degrading tendency of MB. The fabricated NCs were mixed with dye and placed in the dark under stirring, to check the dye adsorption ability of the NCs (Figure 8). Then, the sample and dye mixtures were exposed to the sunlight, to verify their photocatalytic efficiencies against the model pollutant. In the composite photocatalyst series, 70%SGCN/Te@NiS deteriorated MB faster (97%) than the other composites (Figure 8a).



**Figure 8.** Degradation efficiency (a). Kinetic study of photocatalytic degradation of MB by SGCN/Te@NiS NCs (b).

All of the synthetic photocatalysts were found to adhere to first-order kinetics (Figures 7b and 8b). The following sequence of kinetic rates was determined from the pseudo-first-order reaction: SGCN/Te@NiS > Te@NiS > NiS. The 70% SGCN is naturally the best concentration for the SGCN/Te@NiS NC, to achieve its highest photocatalytic activity. Additionally, a rise in SGCN concentration (< 70%) may result in e–h pair combination centers, which gradually reduce photocatalytic efficiency. The fact that the kinetic rate of SGCN/Te@NiS was higher than that of Te@NiS and NiS, suggests that SGCN/Te@NiS has outstanding photocatalytic activity against MB. The photocatalytic activity of the 7% SGCN/Te@NiS NC was found to be better than that of some recent reported composites, because SGCN and Te@NiS might successfully develop good heterojunctions [55–61] (Table 1). Te atoms may also aid in the transport and separation of e<sup>–</sup> and h<sup>+</sup> in the composite.

**Table 1.** Photocatalytic efficiency of the SGCN/Te@NiS NCs and some previously reported work.

Sr. No	Photocatalyst	Target Pollutant	Light Source	Radiation Time (min.)	Degradation %	Ref
1	ZnS	MB	Xe lamp	120	77.2	[69]
2	MgS/Ag <sub>2</sub> MoO <sub>4</sub>	MB	Visible	200	90	[70]
3	BiSbO <sub>4</sub>	MB	Xe lamp	10 h	96.7	[71]
4	FeOOH-LDO	MB	Xe lamp	180	92	[72]
5	BiSbO <sub>4</sub>	MB	Xe lamp	10 h	96.7	[71]
6	Cr-ZnFe <sub>2</sub> O <sub>4</sub> /S-g-C <sub>3</sub> N <sub>4</sub>	MB	Solar	90	100	[73]
7	Pt-BiFeO <sub>3</sub>	MG	Solar	240	96	[74]
8	Co-SnO <sub>2</sub> /SGCN	MB	Solar	120	98	[75]
9	SGCN/Te@NiS	MB	Solar	70	97	Present Work

The EPR spectra of 70%SGCN/1%Te@NiS NCs were studied, to further corroborate the validation of the functional species  $\cdot\text{O}_2^-$  and  $\cdot\text{OH}$  in the photocatalysis event (Figure 9a,b). Although the signals are not visible in the dark, the obvious ESR signals are associated with the  $\text{DMPO}^- \cdot\text{OH}$  and  $\text{DMPO}^- \cdot\text{O}_2^-$  adducts under sunlight, indicating that both  $\cdot\text{OH}$  and  $\cdot\text{O}_2^-$  are formed during the photocatalysis reaction. The EPR results not only confirm the development of the 70%SGCN/1%Te@NiS NCs, but also show how effective the self-assembled approach, built using SGCN/Te@NiS, is for pollutant degradation.

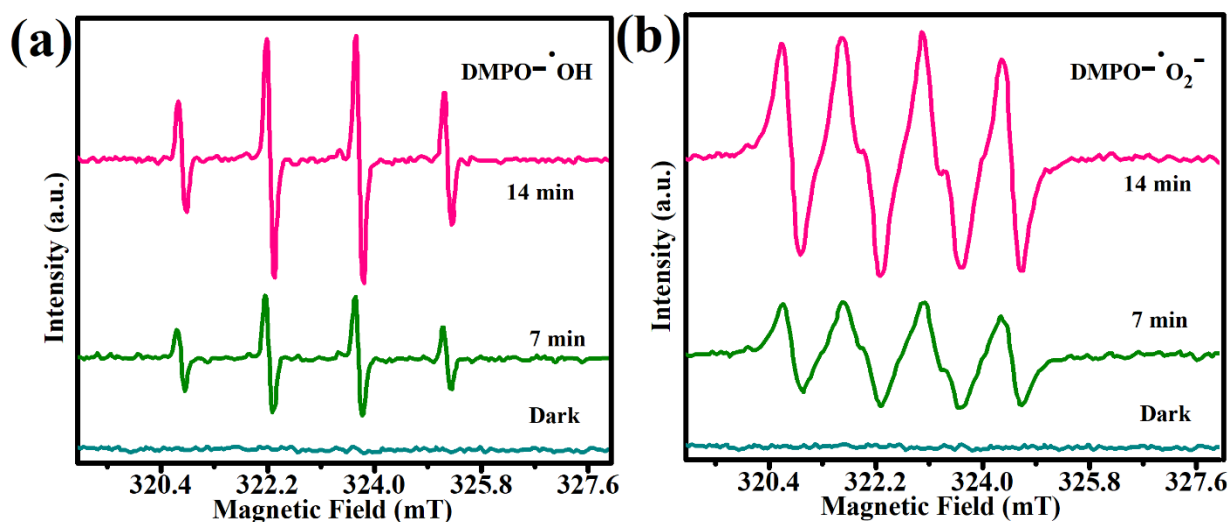


**Figure 9.** 70%SGCN/1%Te@NiS NCs ESR spectra. For  $\text{DMPO}^- \cdot\text{OH}$  (a), this was performed in an aqueous suspension, and for  $\text{DMPO}^- \cdot\text{O}_2^-$  (b) this was performed in a methanol suspension.

### 3.7. Antimicrobial Activity

The antimicrobial activity was explored by using various concentrations of NiS, Te-doped NiS nanoparticles, and composites (100, 200, 300, 400, and 500 mg/L solutions), against two bacteria (*B.subtilis* and *E. coli*) and two fungi (*M. laxa* and *F. oxysporum*) strains. The corresponding bactericidal results were noted by measuring the zone of inhibition (ZOI) and are given in Table 2. It was noted that the SGCN/Te@NiS with a concentration of 500 mg/L showed excellent antibacterial behavior and produces a  $19 \pm 0.8$  mm ZOI against *Bacillus subtilis*, and  $18 \pm 0.8$  mm ZOI against *E. coli* (Table 2). The ordered bactericidal effect of the samples against bacteria was found to be NiS < Te@NiS < SGCN/Te@NiS. According to the proposed photocatalytic and bactericidal mechanism, the synthesized nanocatalysts generate  $e^-/h^+$  pairs and reactive oxygen species (ROS) under light irradiation (Figure 10) [76,77]. The maximal zone of inhibition values of 3Te-ZnO@40SCN NCs, for *M. laxa* and *F. oxysporum*, are 39.2 mm and 36.5 mm, respectively, according to the antifungal potential data (Table 2). The resulting reactive species cause the degradation of the dye and the damage to the cellular membrane, which leads to the death of the microbial cell [78]. In the SGCN/Te@NiS composite, SGCN acts as an electron acceptor, which helps with charge transfer and separates charge carriers, to slow down the rate of recombination. The prolonged lifetime of the  $e^-/h^+$  pair, produces more radicals, which enhances the bactericidal activity of the SGCN/Te@NiS composite. Thus, the improved antibacterial behavior of composites refers to the synergistic effect of the Te@NiS and SGCN substrates. As a result, SGCN/Te@NiS NCs could be used in future pollution remediation and antimicrobial applications.

**Table 2.** NiS, Te@NiS, SGCN, and SGCN/Te@NiS NCs have zones of inhibition for their antifungal potential when employed in the agar-well diffusion method.

Antibacterial and Antifungal Potential			
Bacterial strains	Samples	Blank	Zone of Inhibition (mm)
<i>B. subtilis</i>	NiS	0	11
	Te@NiS	0	13
	SGCN	0	15
	SGCN/Te@NiS	0	19
<i>E. coli</i>	NiS	0	10
	Te@NiS	0	12
	SGCN	0	14
	SGCN/Te@NiS	0	18
<i>M. laxa</i>	NiS	0	15.6
	Te@NiS	0	21.4
	SGCN	0	22.7
	SGCN/Te@NiS	0	39.2
<i>F. oxysporum</i>	NiS	0	13.8
	Te@NiS	0	19.1
	SGCN	0	21.9
	SGCN/Te@NiS	0	36.5

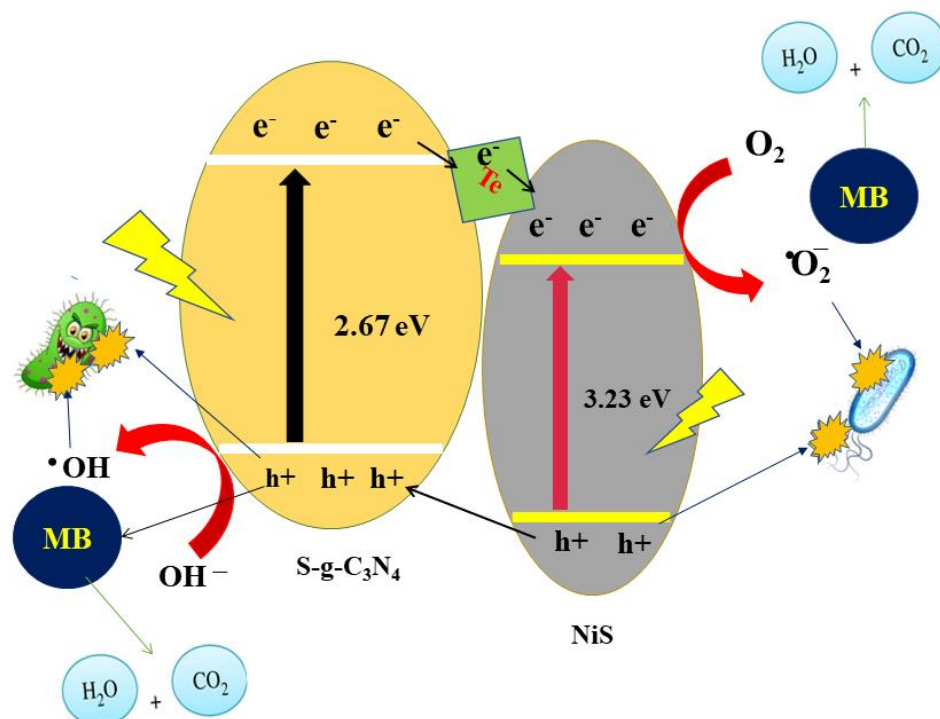


**Figure 10.** Schematic antimicrobial and catalytic dye degradation mechanisms under sunlight of the SGCN/Te@NiS NCs.

#### 4. Conclusions

In this study, a series of Te-doped nickel sulfides were made, by adding tellurium as an impurity (wt.%), and a series of composites were made, by integrating different

concentrations (wt.%) of SGCN into 1%Te@NiS. The successful syntheses of NiS, Te@NiS, and SGCN/1Te@NiS were examined by various characterization techniques, where XRD results confirmed crystallinity, SEM checked the structural morphologies, EDX verified the elemental composition, and FTIR spectra validated the presence of functional groups. The antimicrobial and photocatalytic efficiency of the synthesized samples was checked against bacteria, fungi and MB, respectively. The photocatalytic activity and antimicrobial results showed that the 70%SGCN/1%Te@NiS nanocomposite is an efficient photocatalyst. Further, the good photocatalytic efficiency of the NCs was validated by applying a kinetic study. The Te doping and coupling of SGCN with NiS material, played a vital role in improving the efficiency of the SGCN/Te@NiS NCs. Consequently, the SGCN/Te@NiS NC is a promising material, with prospective uses in water disinfection and purification via photocatalytic decomposition of contaminants.

**Supplementary Materials:** The following supporting information can be downloaded at: <https://www.mdpi.com/article/10.3390/inorganics11040156/s1>, Figure S1: High-resolution S 2p XPS spectrum of 70%SGCN/1%Te@NiS NCs.

**Author Contributions:** Conceptualization, writing-original draft preparation, M.R. and M.J.; validation, performed major experimental works, supervision, S.I.; methodology, software, acquisition of data, A.A.; Q.M.; data curation, design of study, K.A., A.B. and M.A.Q.; reviewed original manuscript and critical revision, N.S.A. and H.A.I.; writing reviewing and editing, software, acquisition of funding, M.M.A.-A. and E.B.E. All authors have read and agreed to the published version of the manuscript.

**Funding:** The authors express their appreciation to the Deanship of Scientific Research at King Khalid University, Saudi Arabia, for funding this work through research group program under grant number RGP.2/273/44. This research was funded by Princess Nourah bint Abdulrahman University Researchers Supporting Project number (PNURSP2023R7), Princess Nourah bint Abdulrahman University, Riyadh, Saudi Arabia.

**Data Availability Statement:** The datasets generated during and/or analyzed during the current study are available from the corresponding author upon reasonable request.

**Acknowledgments:** The authors express their appreciation to the Deanship of Scientific Research at King Khalid University, Saudi Arabia, for funding this work through research group program under grant number RGP.2/273/44. This research was funded by Princess Nourah bint Abdulrahman University Researchers Supporting Project number (PNURSP2023R7), Princess Nourah bint Abdulrahman University, Riyadh, Saudi Arabia.

**Conflicts of Interest:** The authors declare no conflict of interest.

## References

1. Aldalbahi, A.; El-Naggar, M.E.; El-Newehy, M.H.; Rahaman, M.; Hatshan, M.R.; Khattab, T.A. Effects of technical textiles and synthetic nanofibers on environmental pollution. *Polymers* **2021**, *13*, 155. [CrossRef] [PubMed]
2. Khan, A.A.; Khan, M. Pakistan textile industry facing new challenges. *Res. J. Int. Stud.* **2010**, *14*, 21–29.
3. Memon, J.A.; Aziz, A.; Qayyum, M. The rise and fall of Pakistan's textile industry: An analytical view. *Eur. J. Bus. Manag.* **2020**, *12*, 136–142.
4. Singh, S.; Khajuria, R. Penicillium enzymes for the textile industry. In *New and Future Developments in Microbial Biotechnology and Bioengineering*; Elsevier: Amsterdam, The Netherlands, 2018; pp. 201–215.
5. Lellis, B.; Fávoro-Polonio, C.Z.; Pamphile, J.A.; Polonio, J.C. Effects of textile dyes on health and the environment and bioremediation potential of living organisms. *Biotechnol. Res. Innov.* **2019**, *3*, 275–290. [CrossRef]
6. Mansoor, S.; Shahid, S.; Ashiq, K.; Alwadai, N.; Javed, M.; Iqbal, S.; Fatima, U.; Zaman, S.; Nazim Sarwar, M.; Alshammari, F.H.; et al. Controlled growth of nanocomposite thin layer based on Zn-Doped MgO nanoparticles through Sol-Gel technique for biosensor applications. *Inorg. Chem. Commun.* **2022**, *142*, 109702. [CrossRef]
7. Iqbal, S.; Javed, M.; Qamar, M.A.; Bahadur, A.; Fayyaz, M.; Akbar, A.; Alsaab, H.O.; Awwad, N.S.; Ibrahim, H.A.J.C. Synthesis of Cu-ZnO/Polyacrylic Acid Hydrogel as Visible-Light-Driven Photocatalyst for Organic Pollutant Degradation. *Chem. Sel.* **2022**, *7*, e202103694. [CrossRef]
8. Yaseen, D.; Scholz, M. Textile dye wastewater characteristics and constituents of synthetic effluents: A critical review. *Int. J. Environ. Sci. Technol.* **2019**, *16*, 1193–1226. [CrossRef]
9. Singh, Z.; Chadha, P. Textile industry and occupational cancer. *J. Occup. Med. Toxicol.* **2016**, *11*, 39. [CrossRef]

10. Erkurt, H.A. *Biodegradation of Azo Dyes*; Springer: Berlin/Heidelberg, Germany, 2010.
11. Newman, M. The Science of Pollution (Cuarta). 2015. Available online: <https://bit.ly/33OMYAp> (accessed on 12 December 2022).
12. Rehman, K.; Shahzad, T.; Sahar, A.; Hussain, S.; Mahmood, F.; Siddique, M.H.; Siddique, M.A.; Rashid, M.I. Effect of Reactive Black 5 azo dye on soil processes related to C and N cycling. *PeerJ* **2018**, *6*, e4802. [[CrossRef](#)]
13. Sathiyavimal, S.; Vasantharaj, S.; Bharathi, D.; Saravanan, M.; Manikandan, E.; Kumar, S.S.; Pugazhendhi, A. Biogenesis of copper oxide nanoparticles (CuONPs) using *Sida acuta* and their incorporation over cotton fabrics to prevent the pathogenicity of Gram negative and Gram positive bacteria. *J. Photochem. Photobiol. B Biol.* **2018**, *188*, 126–134. [[CrossRef](#)]
14. Qamar, M.A.; Shahid, S.; Javed, M.; Shariq, M.; Fadhali, M.M.; Madkhali, O.; Ali, S.K.; Syed, I.S.; Awaji, M.Y.; Shakir Khan, M. Accelerated Decoloration of Organic Dyes from Wastewater Using Ternary Metal/g-C<sub>3</sub>N<sub>4</sub>/ZnO Nanocomposites: An Investigation of Impact of g-C<sub>3</sub>N<sub>4</sub> Concentration and Ni and Mn Doping. *Catalysts* **2022**, *12*, 1388. [[CrossRef](#)]
15. Afzal, M.I.; Shahid, S.; Mansoor, S.; Javed, M.; Iqbal, S.; Hakami, O.; Yousef, E.S.; Al-Fawzan, F.F.; Elkaeed, E.B.; Pashameah, R.A.; et al. Fabrication of a Ternary Nanocomposite g-C<sub>3</sub>N<sub>4</sub>/Cu@CdS with Superior Charge Separation for Removal of Organic Pollutants and Bacterial Disinfection from Wastewater under Sunlight Illumination. *Toxics* **2022**, *10*, 657. [[CrossRef](#)] [[PubMed](#)]
16. Lee, S.-Y.; Park, S.-J. TiO<sub>2</sub> photocatalyst for water treatment applications. *J. Ind. Eng. Chem.* **2013**, *19*, 1761–1769. [[CrossRef](#)]
17. Kiwaan, H.; Atwee, T.; Azab, E.; El-Bindary, A. Photocatalytic degradation of organic dyes in the presence of nanostructured titanium dioxide. *J. Mol. Struct.* **2020**, *1200*, 127115. [[CrossRef](#)]
18. Dodoo-Arhin, D.; Asiedu, T.; Agyei-Tuffour, B.; Nyankson, E.; Obada, D.; Mwabora, J. Photocatalytic degradation of Rhodamine dyes using zinc oxide nanoparticles. *Mater. Today Proc.* **2021**, *38*, 809–815. [[CrossRef](#)]
19. Rajendrachari, S.; Taslimi, P.; Karaoglanli, A.C.; Uzun, O.; Alp, E.; Jayaprakash, G.K. Photocatalytic degradation of Rhodamine B (RhB) dye in waste water and enzymatic inhibition study using cauliflower shaped ZnO nanoparticles synthesized by a novel One-pot green synthesis method. *Arab. J. Chem.* **2021**, *14*, 103180. [[CrossRef](#)]
20. Lai, M.T.L.; Lai, C.W.; Lee, K.M.; Chook, S.W.; Yang, T.C.K.; Chong, S.H.; Juan, J.C. Facile one-pot solvothermal method to synthesize solar active Bi<sub>2</sub>WO<sub>6</sub> for photocatalytic degradation of organic dye. *J. Alloys Compd.* **2019**, *801*, 502–510. [[CrossRef](#)]
21. Singh, J.; Kumar, V.; Kim, K.-H.; Rawat, M. Biogenic synthesis of copper oxide nanoparticles using plant extract and its prodigious potential for photocatalytic degradation of dyes. *Environ. Res.* **2019**, *177*, 108569. [[CrossRef](#)]
22. Muthuvel, A.; Jothibas, M.; Manoharan, C. Synthesis of copper oxide nanoparticles by chemical and biogenic methods: Photocatalytic degradation and in vitro antioxidant activity. *Nanotechnol. Environ. Eng.* **2020**, *5*, 14. [[CrossRef](#)]
23. Verma, M.; Singh, K.P.; Kumar, A. Reactive magnetron sputtering based synthesis of WO<sub>3</sub> nanoparticles and their use for the photocatalytic degradation of dyes. *Solid State Sci.* **2020**, *99*, 105847. [[CrossRef](#)]
24. Abdelrahman, E.A.; Hegazey, R.; Kotp, Y.H.; Alharbi, A. Facile synthesis of Fe<sub>2</sub>O<sub>3</sub> nanoparticles from Egyptian insecticide cans for efficient photocatalytic degradation of methylene blue and crystal violet dyes. *Spectrochim. Acta Part A Mol. Biomol. Spectrosc.* **2019**, *222*, 117195. [[CrossRef](#)]
25. Aziz, A.; Ali, N.; Khan, A.; Bilal, M.; Malik, S.; Ali, N.; Khan, H. Chitosan-zinc sulfide nanoparticles, characterization and their photocatalytic degradation efficiency for azo dyes. *Int. J. Biol. Macromol.* **2020**, *153*, 502–512. [[CrossRef](#)]
26. Ahadi, M.; Saber Tehrani, M.; Aberoomand Azar, P.; Waqif Husain, S. Novel preparation of sensitized ZnS nanoparticles and its use in photocatalytic degradation of tetracycline. *Int. J. Environ. Sci. Technol.* **2016**, *13*, 2797–2804. [[CrossRef](#)]
27. Ayodhya, D.; Venkatesham, M.; Santoshi Kumari, A.; Reddy, G.B.; Ramakrishna, D.; Veerabhadram, G. Photocatalytic degradation of dye pollutants under solar, visible and UV lights using green synthesised CuS nanoparticles. *J. Exp. Nanosci.* **2016**, *11*, 418–432. [[CrossRef](#)]
28. Borthakur, P.; Boruah, P.K.; Darabdhara, G.; Sengupta, P.; Das, M.R.; Boronin, A.I.; Kibis, L.S.; Kozlova, M.N.; Fedorov, V.E. Microwave assisted synthesis of CuS-reduced graphene oxide nanocomposite with efficient photocatalytic activity towards azo dye degradation. *J. Environ. Chem. Eng.* **2016**, *4*, 4600–4611. [[CrossRef](#)]
29. Kumar, S.; Ojha, A.K. In-situ synthesis of reduced graphene oxide decorated with highly dispersed ferromagnetic CdS nanoparticles for enhanced photocatalytic activity under UV irradiation. *Mater. Chem. Phys.* **2016**, *171*, 126–136. [[CrossRef](#)]
30. Kakodkar, S.B. Synthesis, characterisation and photocatalytic activity of cadmium sulphide nanoparticles. *Chem. Sci. Trans* **2016**, *5*, 75–78.
31. Ayodhya, D.; Veerabhadram, G. Green synthesis, characterization, photocatalytic, fluorescence and antimicrobial activities of *Cochlospermum gossypium* capped Ag<sub>2</sub>S nanoparticles. *J. Photochem. Photobiol. B Biol.* **2016**, *157*, 57–69. [[CrossRef](#)]
32. Sharma, S.; Khare, N. Hierarchical Bi<sub>2</sub>S<sub>3</sub> nanoflowers: A novel photocatalyst for enhanced photocatalytic degradation of binary mixture of Rhodamine B and Methylene blue dyes and degradation of mixture of p-nitrophenol and p-chlorophenol. *Adv. Powder Technol.* **2018**, *29*, 3336–3347. [[CrossRef](#)]
33. Guo, H.; Ke, Y.; Wang, D.; Lin, K.; Shen, R.; Chen, J.; Weng, W. Efficient adsorption and photocatalytic degradation of Congo red onto hydrothermally synthesized NiS nanoparticles. *J. Nanoparticle Res.* **2013**, *15*, 1475. [[CrossRef](#)]
34. Bharathi, D.; Ranjithkumar, R.; Chandarshekar, B.; Bhuvaneshwari, V. Preparation of chitosan coated zinc oxide nanocomposite for enhanced antibacterial and photocatalytic activity: As a bionanocomposite. *Int. J. Biol. Macromol.* **2019**, *129*, 989–996. [[CrossRef](#)] [[PubMed](#)]
35. Oshida, Y. *Bioscience and Bioengineering of Titanium Materials*; Elsevier: Amsterdam, The Netherlands, 2010.
36. Chen, X.; Zhang, H.; Ci, C.; Sun, W.; Wang, Y. Few-layered boronic ester based covalent organic frameworks/carbon nanotube composites for high-performance K-organic batteries. *ACS Nano* **2019**, *13*, 3600–3607. [[CrossRef](#)] [[PubMed](#)]

37. Qamar, M.A.; Javed, M.; Shahid, S.; Iqbal, S.; Abubshait, S.A.; Abubshait, H.A.; Ramay, S.M.; Mahmood, A.; Ghaithan, H.M. Designing of highly active g-C<sub>3</sub>N<sub>4</sub>/Co@ZnO ternary nanocomposites for the disinfection of pathogens and degradation of the organic pollutants from wastewater under visible light. *J. Nanopart. Res.* **2021**, *9*, 105534. [[CrossRef](#)]
38. Zhang, F.; Wang, X.; Liu, H.; Liu, C.; Wan, Y.; Long, Y.; Cai, Z. Recent advances and applications of semiconductor photocatalytic technology. *Appl. Sci.* **2019**, *9*, 2489. [[CrossRef](#)]
39. Ayodhya, D.; Veerabhadram, G. A review on recent advances in photodegradation of dyes using doped and heterojunction based semiconductor metal sulfide nanostructures for environmental protection. *Mater. Today Energy* **2018**, *9*, 83–113.
40. Iqbal, S. Spatial charge separation and transfer in L-cysteine capped NiCoP/CdS nano-heterojunction activated with intimate covalent bonding for high-quantum-yield photocatalytic hydrogen evolution. *Appl. Catal. B Environ.* **2020**, *274*, 119097. [[CrossRef](#)]
41. Alenizia, M.; Alserourya, F.; Kumarc, R.; Aslamd, M.; Barakatc, M. Removal of trichlorophenol from wastewater using NiS/RGO/TiO. *Composites* **2020**, *24*, 26.
42. Goma, M.M.; Sayed, M.H.; Abdel-Wahed, M.S.; Boshta, M. A facile chemical synthesis of nanoflake NiS 2 layers and their photocatalytic activity. *RSC Adv.* **2022**, *12*, 10401–10408. [[CrossRef](#)]
43. Guo, Y.; Guo, D.; Ye, F.; Wang, K.; Shi, Z. Synthesis of lawn-like NiS<sub>2</sub> nanowires on carbon fiber paper as bifunctional electrode for water splitting. *Int. J. Hydrogen Energy* **2017**, *42*, 17038–17048. [[CrossRef](#)]
44. Xie, Y.; Zhou, Y.; Gao, C.; Liu, L.; Zhang, Y.; Chen, Y.; Shao, Y. Construction of AgBr/BiOBr S-scheme heterojunction using ion exchange strategy for high-efficiency reduction of CO<sub>2</sub> to CO under visible light. *Sep. Purif. Technol.* **2022**, *303*, 122288. [[CrossRef](#)]
45. Sher, M.; Javed, M.; Shahid, S.; Hakami, O.; Qamar, M.A.; Iqbal, S.; AL-Anazy, M.M.; Baghdadi, H.B. Designing of highly active g-C<sub>3</sub>N<sub>4</sub>/Sn doped ZnO heterostructure as a photocatalyst for the disinfection and degradation of the organic pollutants under visible light irradiation. *J. Photochem. Photobiol. A Chem.* **2021**, *418*, 113393. [[CrossRef](#)]
46. Shinde, D.V.; Patil, S.A.; Cho, K.; Ahn, D.Y.; Shrestha, N.K.; Mane, R.S.; Lee, J.K.; Han, S.H. Revisiting Metal Sulfide Semiconductors: A Solution-Based General Protocol for Thin Film Formation, Hall Effect Measurement, and Application Prospects. *Adv. Funct. Mater.* **2015**, *25*, 5739–5747. [[CrossRef](#)]
47. Isac, L.; Cazan, C.; Enesca, A.; Andronic, L. Copper sulfide based heterojunctions as photocatalysts for dyes photodegradation. *Front. Chem.* **2019**, *7*, 694. [[CrossRef](#)] [[PubMed](#)]
48. Zhang, S.; Ou, X.; Xiang, Q.; Carabineiro, S.A.; Fan, J.; Lv, K. Research progress in metal sulfides for photocatalysis: From activity to stability. *Chemosphere* **2022**, 135085. [[CrossRef](#)] [[PubMed](#)]
49. Santhosh, C.; Malathi, A.; Daneshvar, E.; Kollu, P.; Bhatnagar, A. Photocatalytic degradation of toxic aquatic pollutants by novel magnetic 3D-TiO<sub>2</sub>@HPGA nanocomposite. *Sci. Rep.* **2018**, *8*, 1–15. [[CrossRef](#)]
50. Yang, Y.; He, J.; Wu, G.; Hu, J. “Thermal Stabilization Effect” of Al<sub>2</sub>O<sub>3</sub> nano-dopants improves the high-temperature dielectric performance of polyimide. *Sci. Rep.* **2015**, *5*, 1–10. [[CrossRef](#)]
51. Peng, Z.; Lou, S.; Gao, Y.; Kong, L.; Yan, S.; Wang, K.; Song, H. Effect of Co doping on electrocatalytic performance of Co-NiS<sub>2</sub>/CoS<sub>2</sub> heterostructures. *Nanomaterials* **2021**, *11*, 1245. [[CrossRef](#)]
52. Tomke, P.D.; Rathod, V.K. Nanoengineering Tools in Beverage Industry. In *Nanoengineering in the Beverage Industry*; Elsevier: Amsterdam, The Netherlands, 2020; pp. 35–69.
53. Jing, J.; Chen, Z.; Feng, C.; Sun, M.; Hou, J. Transforming g-C<sub>3</sub>N<sub>4</sub> from amphoteric to n-type semiconductor: The important role of p/n type on photoelectrochemical cathodic protection. *J. Alloys Compd.* **2021**, *851*, 156820. [[CrossRef](#)]
54. Mao, M.; Xu, J.; Li, L.; Zhao, S.; Li, X. The pn heterojunction constructed by NiMnO<sub>3</sub> nanoparticles and NiS<sub>4</sub> to promote charge separation and efficient catalytic hydrogen evolution. *Int. J. Hydrogen Energy* **2021**, *46*, 23190–23204. [[CrossRef](#)]
55. Matsuura, K.; Mizumoto, N.; Kobayashi, K.; Nozaki, T.; Fujita, T.; Yashiro, T.; Fuchikawa, T.; Mitaka, Y.; Vargo, E.L. A genomic imprinting model of termite caste determination: Not genetic but epigenetic inheritance influences offspring caste fate. *Am. Nat.* **2018**, *191*, 677–690. [[CrossRef](#)]
56. Fu, J.; Yu, J.; Jiang, C.; Cheng, B. g-C<sub>3</sub>N<sub>4</sub>-Based Heterostructured Photocatalysts. *Adv. Energy Mater.* **2017**, *8*, 1701503. [[CrossRef](#)]
57. Luo, X.-L.; He, G.-L.; Fang, Y.-P.; Xu, Y.-H. Nickel sulfide/graphitic carbon nitride/strontium titanate (NiS/g-C<sub>3</sub>N<sub>4</sub>/SrTiO<sub>3</sub>) composites with significantly enhanced photocatalytic hydrogen production activity. *J. Colloid Interface Sci.* **2018**, *518*, 184–191. [[CrossRef](#)] [[PubMed](#)]
58. Li, Y.; Li, X.; Wang, X.-T.; Jian, L.-J.; Abdallah, N.I.M.; Dong, X.-F.; Wang, C.-W. Pn Heterostructured design of decahedral NiS/BiVO<sub>4</sub> with efficient charge separation for enhanced photodegradation of organic dyes. *Colloids Surf. A Physicochem. Eng. Asp.* **2021**, *608*, 125565. [[CrossRef](#)]
59. Vignesh, S.; Kim, H. Interfacial coupling effects in α-Fe<sub>2</sub>O<sub>3</sub>/g-C<sub>3</sub>N<sub>4</sub> composite magnetically separable heterojunction with upgraded Z-scheme photocatalytic performance of mixed organic pollutant degradation. *J. Phys. Chem. Solids* **2022**, *169*, 110869. [[CrossRef](#)]
60. Vinoth, S.; Rajaiatha, P.M.; Venkadesh, A.; Devi, K.S.; Radhakrishnan, S.; Pandikumar, A. Nickel sulfide-incorporated sulfur-doped graphitic carbon nitride nanohybrid interface for non-enzymatic electrochemical sensing of glucose. *Nanoscale Adv.* **2020**, *2*, 4242–4250. [[CrossRef](#)]
61. Javed, M.; Abid, M.; Hussain, S.; Shahwar, D.; Arshad, S.; Ahmad, N.; Arif, M.; Khan, H.; Nadeem, S.; Raza, H. Synthesis, characterization and photocatalytic applications of s-doped graphitic carbon nitride nanocomposites with nickel doped zinc oxide nanoparticles. *Dig. J. Nanomater. Biostruct.* **2020**, *15*, 1097–1105. [[CrossRef](#)]

62. Mi, L.; Chen, Y.; Wei, W.; Chen, W.; Hou, H.; Zheng, Z. Large-scale urchin-like micro/nano-structured NiS: Controlled synthesis, cation exchange and lithium-ion battery applications. *RSC Adv.* **2013**, *3*, 17431–17439. [[CrossRef](#)]
63. Pitchaiya, S.; Natarajan, M.; Santhanam, A.; Ramakrishnan, V.M.; Asokan, V.; Palanichamy, P.; Rangasamy, B.; Sundaram, S.; Velauthapillai, D. Nickel sulphide-carbon composite hole transporting material for (CH<sub>3</sub>NH<sub>3</sub>PbI<sub>3</sub>) planar heterojunction perovskite solar cell. *Mater. Lett.* **2018**, *221*, 283–288. [[CrossRef](#)]
64. Wang, K.; Li, Q.; Liu, B.; Cheng, B.; Ho, W.; Yu, J. Sulfur-doped g-C<sub>3</sub>N<sub>4</sub> with enhanced photocatalytic CO<sub>2</sub>-reduction performance. *Appl. Catal. B Environ.* **2015**, *176–177*, 44–52. [[CrossRef](#)]
65. Abubshait, S.A.; Iqbal, S.; Abubshait, H.A.; AlObaid, A.A.; Al-Muhimeed, T.I.; Abd-Rabboh, H.S.; Bahadur, A.; Li, W.J.C.; Physicochemical, S.A.; Aspects, E. Effective heterointerface combination of 1D/2D Co-NiS/Sg-C<sub>3</sub>N<sub>4</sub> heterojunction for boosting spatial charge separation with enhanced photocatalytic degradation of organic pollutants and disinfection of pathogens. *Colloids Surf. A Physicochem. Eng. Asp.* **2021**, *628*, 127390. [[CrossRef](#)]
66. Iqbal, S.; Bahadur, A.; Javed, M.; Liu, G.; Al-Muhimeed, T.I.; AlObaid, A.A.; Ahmad, Z.; Feng, K.; Xiao, D.J. Synergetic intimate interface contacts of 2D/1D Sg-C<sub>3</sub>N<sub>4</sub>/Co-NiS heterojunction with spatial charge separation for boosting photodegradation of MB and inactivation of pathogens under visible light irradiation. *J. Alloys Compd.* **2022**, *892*, 162012. [[CrossRef](#)]
67. Bahadur, A.; Iqbal, S.; Alsaab, H.O.; Awwad, N.S.; Ibrahim, H.A. Designing a novel visible-light-driven heterostructure Ni-ZnO/SgC 3 N 4 photocatalyst for coloured pollutant degradation. *RSC Adv.* **2021**, *11*, 36518–36527. [[CrossRef](#)] [[PubMed](#)]
68. Iqbal, S.; Amjad, A.; Javed, M.; Alfakeer, M.; Mushtaq, M.; Rabea, S.; Elkaeed, E.B.; Pashameah, R.A.; Alzahrani, E.; Farouk, A.-E. Boosted Spatial Charge Carrier Separation of Binary ZnFe<sub>2</sub>O<sub>4</sub>/Sg-C<sub>3</sub>N<sub>4</sub> Heterojunction for Visible-light-driven Photocatalytic activity and Antimicrobial Performance. *Front. Chem.* **2022**, *894*. [[CrossRef](#)]
69. Ye, Z.; Kong, L.; Chen, F.; Chen, Z.; Lin, Y.; Liu, C. A comparative study of photocatalytic activity of ZnS photocatalyst for degradation of various dyes. *Optik* **2018**, *164*, 345–354. [[CrossRef](#)]
70. Kokilavani, S.; Syed, A.; Kumar, B.H.; Elgorban, A.M.; Bahkali, A.H.; Ahmed, B.; Das, A.; Khan, S.S. Facile synthesis of MgS/Ag<sub>2</sub>MoO<sub>4</sub> nanohybrid heterojunction: Outstanding visible light harvesting for boosted photocatalytic degradation of MB and its anti-microbial applications. *Colloids Surf. A Physicochem. Eng. Asp.* **2021**, *627*, 127097. [[CrossRef](#)]
71. Lin, X.P.; Huang, F.Q.; Wang, W.D.; Zhang, K.L. A novel photocatalyst BiSbO<sub>4</sub> for degradation of methylene blue. *Appl. Catal. A Gen.* **2006**, *307*, 257–262. [[CrossRef](#)]
72. Wang, C.; Zhu, L.; Chang, C.; Fu, Y.; Chu, X. Preparation of magnetic composite photocatalyst Bi<sub>2</sub>WO<sub>6</sub>/CoFe<sub>2</sub>O<sub>4</sub> by two-step hydrothermal method and its photocatalytic degradation of bisphenol A. *Catal. Commun.* **2013**, *37*, 92–95. [[CrossRef](#)]
73. Zhang, P.; Munawar, T.; Soltane, R.; Javed, M.; Liu, G.; Iqbal, S.; Qamar, M.A.; Dera, A.A.; Alrbyawi, H.; Alfakeer, M. Fabrication of Cr-ZnFe<sub>2</sub>O<sub>4</sub>/Sg-C<sub>3</sub>N<sub>4</sub> Heterojunction Enriched Charge Separation for Sunlight Responsive Photocatalytic Performance and Antibacterial Study. *Molecules* **2022**, *27*, 6330. [[CrossRef](#)]
74. Jaffari, Z.H.; Lam, S.-M.; Sin, J.-C.; Zeng, H.; Mohamed, A.R. Magnetically recoverable Pd-loaded BiFeO<sub>3</sub> microcomposite with enhanced visible light photocatalytic performance for pollutant, bacterial and fungal elimination. *Sep. Purif. Technol.* **2020**, *236*, 116195. [[CrossRef](#)]
75. Javed, M.; Iqbal, S.; Qamar, M.A.; Shariq, M.; Ahmed, I.A.; BaQais, A.; Alzahrani, H.; Ali, S.K.; Masmali, N.; Althagafi, T.M. Fabrication of Effective Co-SnO<sub>2</sub>/SGCN Photocatalysts for the Removal of Organic Pollutants and Pathogen Inactivation. *Crystals* **2023**, *13*, 163. [[CrossRef](#)]
76. Qamar, M.A.; Shahid, S.; Javed, M.; Iqbal, S.; Sher, M.; Bahadur, A.; AL-Anazy, M.M.; Laref, A.; Li, D. Designing of highly active g-C<sub>3</sub>N<sub>4</sub>/Ni-ZnO photocatalyst nanocomposite for the disinfection and degradation of the organic dye under sunlight radiations. *Colloids Surf. A Physicochem. Eng. Asp.* **2021**, *614*, 126176. [[CrossRef](#)]
77. Elavarasan, N.; Vignesh, S.; Srinivasan, M.; Venkatesh, G.; Palanisamy, G.; Ramasamy, P.; Palanivel, B.; Al-Enizi, A.M.; Ubaidullah, M.; Reddy, V.R.M. Synergistic S-Scheme mechanism insights of g-C<sub>3</sub>N<sub>4</sub> and rGO combined ZnO-Ag heterostructure nanocomposite for efficient photocatalytic and anticancer activities. *J. Alloys Compd.* **2022**, *906*, 164255. [[CrossRef](#)]
78. Qamar, M.A.; Shahid, S.; Javed, M.; Iqbal, S.; Sher, M.; Akbar, M.B. Highly efficient g-C<sub>3</sub>N<sub>4</sub>/Cr-ZnO nanocomposites with superior photocatalytic and antibacterial activity. *J. Photochem. Photobiol. A Chem.* **2020**, *401*, 112776. [[CrossRef](#)]

**Disclaimer/Publisher's Note:** The statements, opinions and data contained in all publications are solely those of the individual author(s) and contributor(s) and not of MDPI and/or the editor(s). MDPI and/or the editor(s) disclaim responsibility for any injury to people or property resulting from any ideas, methods, instructions or products referred to in the content.